Materials Research, Vol. 7, No. 4, 557-564, 2004.

Ceramic Foams Porous Microstructure Characterization By X-ray Microtomography

Carlos Roberto Appoloni[a]*, *Celso Peres Fernandes*[b], *Murilo Daniel de Mello Innocentini*[c], *Álvaro Macedo*[d]

[a]*Departamento de Física, Universidade Estadual de Londrina*
C.P. 6001, 86051-990 Londrina - PR, Brazil
[b]*LMPT, Departamento de Engenharia Mecânica, Universidade Federal de Santa Catarina*
C.P. 476, 88040-900 Florianópolis - SC, Brazil
[c]*Grupo de Engenharia de Microestrutura de Materiais (GEMM), Departamento de Engenharia de Materiais, Universidade Federal de São Carlos - SP, Brazil*
[d]*Embrapa Instrumentação Agropecuária*
C.P. 741, 13560-970 São Carlos - SP, Brazil

Received: January 23, 2004; Revised: June 29, 2004

Knowledge of the porous structure of amorphous materials is of fundamental importance in calculating geometrical parameters such as total porosity, pore size distribution and physical parameters relating to fluid flow inside void space. The present work deals with the measurement of the microstructural parameters of porous ceramic filters. Microtomographic measurements of samples were taken using an X-ray tube. Bremsstrahlung radiation was filtered in transmission mode with a Sn filter at 58.5 and 28.3 keV and the images analyzed in two ways. The first method consisted in analyzing transepts of the images in order to calculate total porosity based on the average particle size and media linear attenuation coefficients. The second method involved a study of the images using an image analysis software, called Imago, which allows one to calculate total porosity and pore size distribution. The total measured porosity of the filter C90 was 73.8%, 71.1%, 74.4% and 71.5% by, respectively, the Arquimedes method, simple gamma ray transmission, transept analysis and analysis of the microtomographic images at 28.3 keV.

Keywords: *microstructure, ceramic foams, microtomography, X-ray*

1. Introduction

Millimetric scale X and gamma ray computerized tomography (CT) has been used in many fields of application since its development for medical diagnoses in 1973. More recently, the need to look inside porous media at the level of pores and aggregates in order to observe the topology and geometry of the pores, as well as other applications, led to the development of micrometric scale tomography. This implied a specific study of radiation sources, detectors, collimators, mechanics, hardware and software to design dedicated systems for different fields such as archaeometry, soil physics, porous materials and other applications[1,2].

Knowledge of the porous structure of amorphous materials is required to calculate microstructural parameters, such as pore size distribution and total porosity, and important for deriving the physical parameters of fluid flow in the sample, such as permeability. In this sense, the first possibility is to use 2D images to extract statistical descriptors of the pore space morphology, such as porosity and autocorrelation functions. These descriptors may be used directly to search for empirical correlations with the transport properties[3]. Alternatively, the statistical properties obtained from a cross-section may be used to constrain the generation of a 3D pore space[4-6]. Direct simulation of 3D flow in the reconstructed pore space may be performed using Navier-Stokes equations[7] or lattice gas/lattice Boltzmann simulations[8].

A nondestructive way to obtain the statistical descriptors of porous geometries is to take microtomographic meas-

*e-mail: appoloni@uel.br

urements of the samples and analyze the images to extract the information of interest. The importance of the methodology employed in this work, which is based on image analyses of microtomographic measurements, is that it allows one to measure several morphological and topological descriptors of the microstructure that are difficult to obtain or not accessible by conventional techniques.

The purpose of this work was to obtain the microstructural parameters of ceramic foams using X-ray microtomography and image analysis.

2. Materials and Methods

The equipment used was a first generation X-ray tomograph with micrometric resolution[9]. The X-ray tube comprised a W anode and 3 kW tube operated at 70 kV/10 mA and at 50 kV/23 mA for two different energy conditions. A transmission energy filter of Sn was employed to obtain almost monochromatic lines[1,10] of 58.5 and 28.3 keV. Collimators of 60 μm and 215 μm were used at the NaI (Tl) detector entrance and the tube output, respectively. The beam width at the sample position was about 80 μm. The linear step of the projection measurements varied from 53.3 to 57.8 μm and the angular step was 0.8°. The number of projections was 225 and the scanning time for each projection was 5 s. Figure 1 shows a block diagram of the CT scanner.

The data matrix was processed by the "Microvis" reconstruction software developed at the Instrumentation Center of the Brazilian Enterprise for Agricultural Research Corporation (EMBRAPA). The Microvis software reconstructs the image by applying the filtered backprojection algorithm, in which the projections are initially transferred to the frequency domain and then bandlimited through the application of a filter. These filtered projections are brought back to the space domain and summed up to give the distribution of the linear attenuation coefficient values, in other words, to compose the image of the sample section[9,11].

The microtomographies obtained were processed using the "Imago" image analysis software to determine total porosity, the autocorrelation function and pore size distribution. Imago was developed at the Laboratory of Porous Media and Thermophysical Properties (LMPT), Department of Mechanical Engineering, Federal University of Santa Catarina in association with Engineering Simulation and Scientific Software (ESSS).

The original gray-level microtomographies were processed with the "Imago" software to produce binary images after segmentation of the pore and solid phases. This procedure is based on the gray-level histogram, where the user selects the threshold that appears to best separate the gray-level classes associated with solid and porous phases.

The porous media represented in a 2-D binary image can be characterized by the pore phase function Z **(x)** as follows:

$$Z(\mathbf{x}) = \begin{cases} 1 & \text{when } \mathbf{x} \text{ belongs to the pore space} \\ 0 & \text{otherwise} \end{cases} \quad (1)$$

where **x** denotes the position with respect to an arbitrary origin.

The porosity, ϕ, the autocorrelation function, C (**u**), and the normalized autocorrelation function, R (**u**), can be defined, respectively, by the following statistical averages (de-

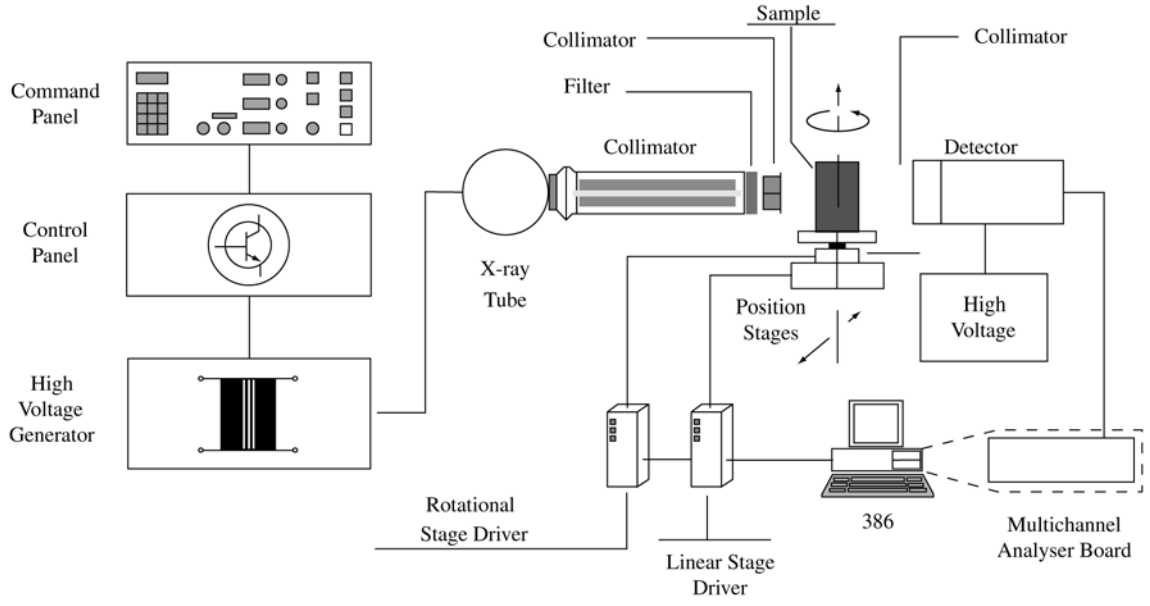

Figure 1. Block diagram of the CT scanner.

noted by $\langle\ \rangle$):

$$\phi = \langle Z(\mathbf{x}) \rangle \tag{2}$$

$$C(\mathbf{u}) = \langle Z(\mathbf{x}) Z(\mathbf{x}+\mathbf{u}) \rangle \tag{3}$$

$$R(\mathbf{u}) = \frac{\langle [Z(\mathbf{x})-\phi][Z(\mathbf{x}+\mathbf{u})-\phi] \rangle}{\phi - \phi^2} \tag{4}$$

where **u** is the displacement in the plane of the image.

Porosity, ϕ, is obviously a positive quantity limited to the [0-1] interval. When the media is homogeneous, the statistical parameters are independent of position **x** in space. Thus, the porosity is constant and R (**u**) depends only upon the vector **u** being independent of position **x**.

Moreover, when the porous media is isotropic, R_z is a function only of u = |**u**| and does not depend on the direction of **u**.

The correlation function can be calculated directly in the image domain[12]. Let S be a section of a porous medium, given by a 2D binary representation, with the porous phase represented in black and the solid matrix in white. The binary image, S, is divided into two halves, S_1 and S_2. Hence,

$$S = S_1 \cup S_2,\ S_1 \cap S_2 = \varnothing \tag{5}$$

In order to calculate $R_z(u)$, S_1 is first translated by a distance u along the x-axis; yielding $S_1(+ u)$. The spatial average indicated in Eq. 3 is calculated as an intersection of images, giving the correlation function.

$$\overline{Z(x,y) \cdot Z(x+u,y)} = S_1(+ u) \cap S \tag{6}$$

C(u) relates to the *probability* of finding two points (pixels) separated by u and belonging to the same phase.

Liang *et al.*[5] calculated the autocorrelation function C (**u**) as a function of the two-dimensional vector **u** = (x,y) and then calculated its mean value around a circle with radius u = |**u**|. This procedure produces more reliable C (u) values because it increases the number of realizations needed to calculate this probability.

For an image f (x,y), the Fourier transform of the autocorrelation function is the power spectrum of f (x,y) (Wiener-Khinchin theorem). Thus, with the Fourier transform of the image, the correlation function can be obtained rapidly performing the inverse Fourier transform of the power spectrum. The 2D autocorrelation function is calculated by Imago using the Fourier transform. Fluctuations in the autocorrelation function are drastically reduced when C (u) is calculated by Fourier transform, compared with above described spatial method.

The pore size distribution is obtained by successive openings derived from mathematical morphology[13], using balls with increasing radius. After an opening operation with a given ball radius r, the resulting image can be viewed as the union of radius-r balls completely enclosed in the porous phase. In this way, after opening, the porous phase loses all the features that can be eroded by a given radius-r opening ball. The cumulative porous distribution is given by:

$$F(r) = \frac{\phi - \phi(r)}{\phi} \tag{7}$$

where f is the total porosity of the original image and ϕ (r) is the volume fraction of the porous phase after opening with a radius-r ball.

To reduce the processing time, the opening operation is not applied directly to the binary image but to a transformed image called background distance image**.** In this image, each pixel is labeled with its smallest distance to the neighboring background. This labeling technique uses a sequential algorithm[14], in which the Euclidean distance is approximated by a discrete integer distance. The most commonly used discrete distance is the chamfer distance, known as $d_{3\text{-}4}$, in which each neighbor from a given point, which is taken following the horizontal and vertical coordinate axis, is considered to be 3 measuring units distant from the starting point. The diagonal neighbors are considered to be at 4 measuring units from that point. Thus, this discrete distance gives the numerical approximation of 4/3 = 1.333...to the square root of 2 (1.4142...). The main advantage of using this discrete distance is that it requires lower computer storage space, since only integers are stored in the resident memory.

The total porosity was also determined by other methods.

Through various transept analyses of each microtomography, the total porosity was calculated by means of the linear attenuation coefficients at particle density and average medium, as follows:

$$P_t = 100\left(\frac{\mu_p - \mu_m}{\mu_p}\right) \tag{8}$$

where μ_m is the average medium linear attenuation coefficient of the transept considered in the tomography and μ_p is the average particle linear attenuation coefficient of the transept.

For purposes of comparison, results from conventional methodologies such as Arquimedes, Hg and gas porosimetry were also employed, as well as the single gamma ray transmission technique.

Three kinds of SiC-Al_2O_3 ceramic foams used for solid-fluid separation in the metallurgical, automotive and petrochemical industries were studied: 60 ppi, 75 ppi and 90 ppi (ppi = pores per linear inch). The foams were supplied by the Microstructural Materials Engineering Group (GEMM), Materials Engineering Department, Federal University of São Carlos. The microtomographies of these

samples were performed at 28.3 keV. Figure 2 illustrates the three types of samples.

3. Results

Figures 3 to 5 show CT images obtained at 28.3 kev for the 60 ppi (9 × 11 mm^2), 75 ppi (9 × 11mm^2) and 90 ppi ceramic foam samples (5 × 9 mm^2), respectively. Details of the structure, from pores (black areas) to compact particle aggregates (white areas), are clearly visible.

Table 1 lists the porosity results. Each of the three images was divided into two parts and the porosity was determined for both the parts and the entire image. The results show that the 60 ppi image is homogeneous, while the 75 ppi image is somewhat heterogeneous and the 90 ppi image presents important heterogeneities. These heterogeneities can be associated to the scale of the image analysis: possibly, the field of the analyzed image is small compared with the pore size. Therefore, for a more accurate calculation of porosity and other geometrical parameters, larger images may be required (retaining the same spatial resolution) in order to reach the scale of homogeneity of the microstructure, if it really exists. Despite their heterogeneities, the 75 and 90 ppi images were used in this study to determine the geometrical parameters of porosity, autocorrelation function and pore size distribution. This was also done to present the technique of image analysis that allows the microstructure of ceramic samples to be characterized in greater detail. Table 1 shows that, for determining total porosity in the three types of samples, image and transept analysis, gamma ray transmission[15] and the conventional method[15] supplied results in reasonable agreement. For the 60 ppi ceramic foam, only two of the seven total porosity measurements are not within the 95% confidence level interval, and one of these two (89.7%) is very close to the upper level (89.5%). For the 75 ppi ceramic foam, only one of the five measurements is not within the 95% confidence level interval, and even so it is close (92.7%) to the upper level (91.9%). For the 90 ppi ceramic foam, only one of the five measurements is not within

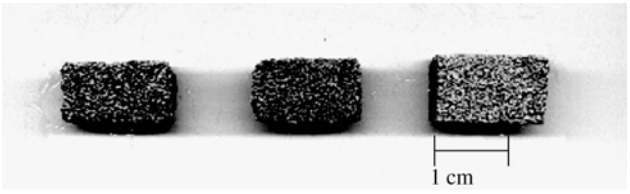

Figure 2. Ceramic foam samples of 60 ppi, 75 ppi and 90 ppi (from left to right).

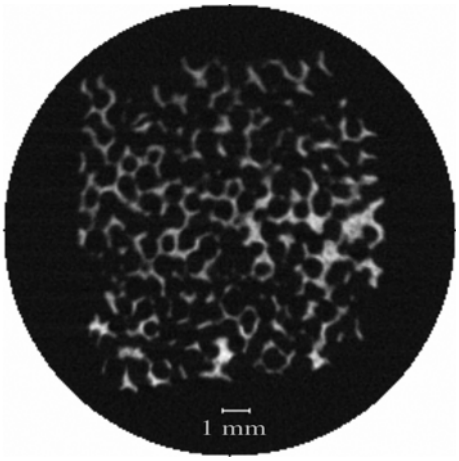

Figure 3. CT image of 60 ppi ceramic sample (9 × 11mm^2) measured at 28.3 keV.

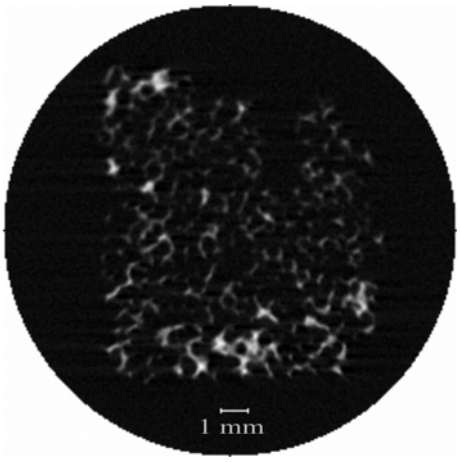

Figure 4. CT image of 75 ppi ceramic sample (9 × 11mm^2) measured at 28.3 keV.

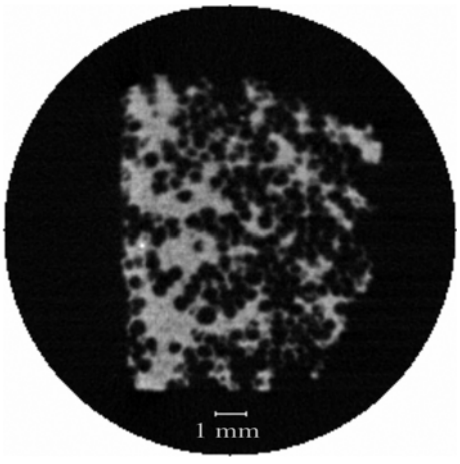

Figure 5. CT image of 90 ppi ceramic sample (5 × 9 mm^2) measured at 28.3 keV.

Table 1. Total Porosity (P_t) of the ceramic foam samples.

METHOD	60 ppi - P_t (%)	75 ppi - P_t (%)	90 ppi - P_t (%)
Archimedes[15]	88.9	87.4	73.8
Gamma Ray transmission[15]	89.7	90.7	71.1
Transept analysis	80.8	86.7	74.4
28.3 keV CT tomography			
Imago analysis	88.9[a] ; 84.6[a]	87.8[a] ; 92.7[a]	71.5[a] ; 56.8[a]
28.3 keV CT tomography	87.8[b] ; 86.4[b]; 87,0[c]		
Average values	86.7	89.1	69.5
95% Confidence Interval	83.9 - 89.5	86.3 - 91.9	61.3 - 77.7
(Student statistics)	(result “c” not considered)		

a) two longitudinal halves; b) two transversal halves; c) whole image.

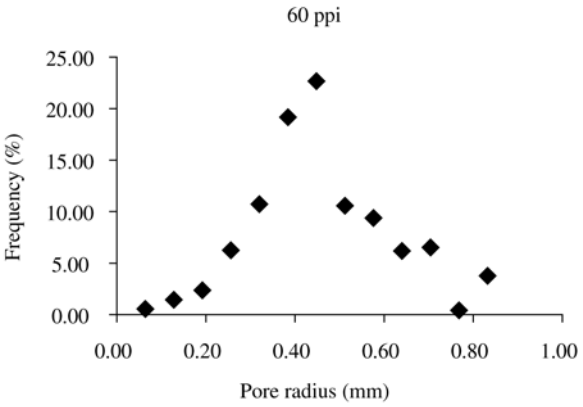

Figure 6. 60 ppi ceramic foam pore size distribution.

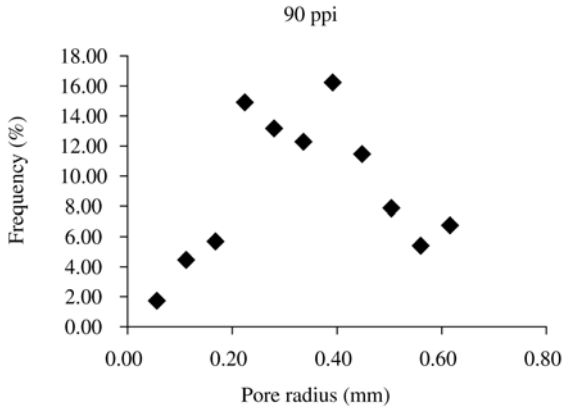

Figure 8. 90 ppi ceramic foam pore size distribution.

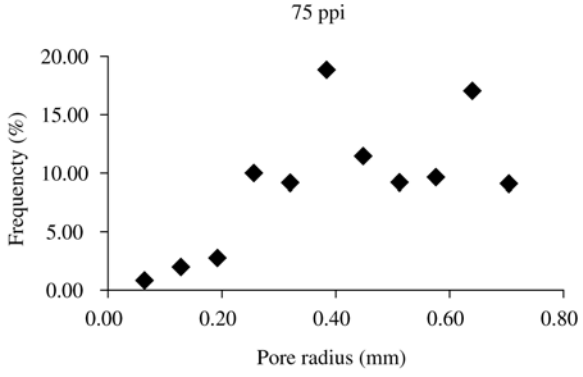

Figure 7. 75 ppi ceramic foam pore size distribution.

the 95% confidence level interval.

Figures 6 to 8 show the pore size distribution in the ceramic foam samples, obtained with Imago analysis. The fig. clearly depicts the range of pore sizes predominating in each type of sample. This kind of data is not usually reported in the literature, because the conventional methods only allow the sample’s average pore radius to be determined. The pore frequency distribution provides a much better characterization of the quality and properties of the ceramic foam. 75.5% of the pores of the 60 ppi ceramic foam had radii ranging from 0.26 to 0.64 mm, but 42% of the pores had radii of 0.38 to 0.45 mm. The 75 ppi ceramic foam displayed no clearly centered pore radius distribution, since 94% of its pores had radii ranging from 0.26 to 0.70 mm. 76% of the pores of the 90 ppi ceramic foam presented radii ranging from 0.22 to 0.50 mm. The two halves of the 75 and 90 ppi samples showed total porosity differing by 6% and 26%, respectively.

Figures 9 to 11 show selected transepts of the samples’ CT images.

Figures 12 to 14 depict the binary images of the samples generated by the Imago software and used for the calculations of porosity and autocorrelation.

Table 2 shows the comparison of present results for ceramic foams samples with data from the literature, which are discussed in an extensive review paper[16] of the area. This review paper, among other data analysis, reports re-

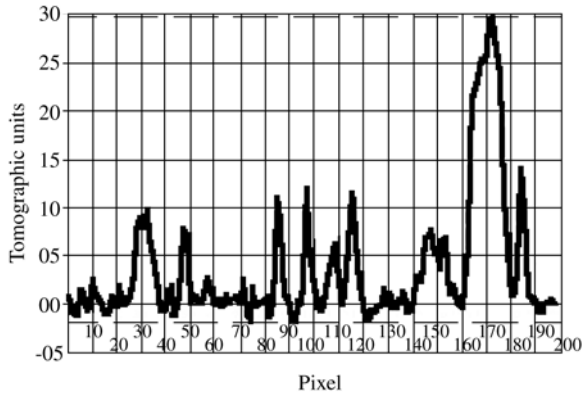

Figure 9. Selected transept of the 60 ppi ceramic sample's CT image.

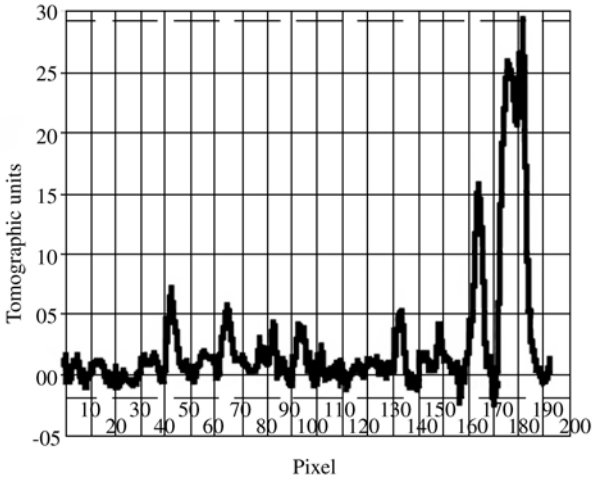

Figure 10. Selected transept of the 75 ppi ceramic sample's CT image.

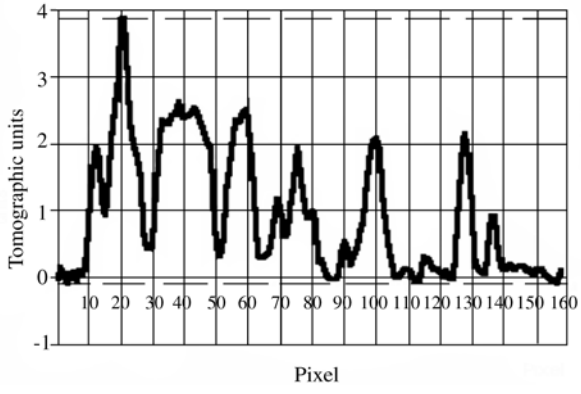

Figure 11. Selected transept of the 90 ppi ceramic sample's CT image.

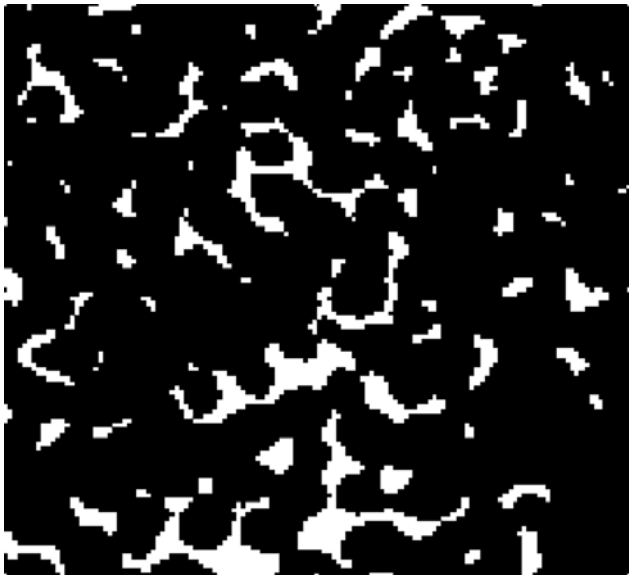

Figure 12. Binary image pattern of the 60 ppi sample.

Figure 13. Binary image pattern of the 75 ppi sample.

sults of twelve different works, published between 1998 and 1985, dealing with ceramic foams produced by the replication technique, concerning the relationship between pore count, porosity and pore size.

There is very good agreement for total porosity results for the three types of ceramic filters.

Average pore size is also shown at Table 2. But, due to the complexity of the porous space geometry, this parameter is strongly model dependent and hardly could be compared.

Figure 15 shows a comparison of the normalized autocorrelation for the 60, 75 and 90 ppi ceramic foams. As can be seen, the correlation-curves resemble each other closely, denoting a similar spatial arrangement. Correlation-length, as defined by Lanteajoul, C.[17]: $\ell = \int_0^\infty R(u)du$, was estimated as 0.30 mm for the three samples.

Figure 14. Binary image pattern of the 90 ppi sample.

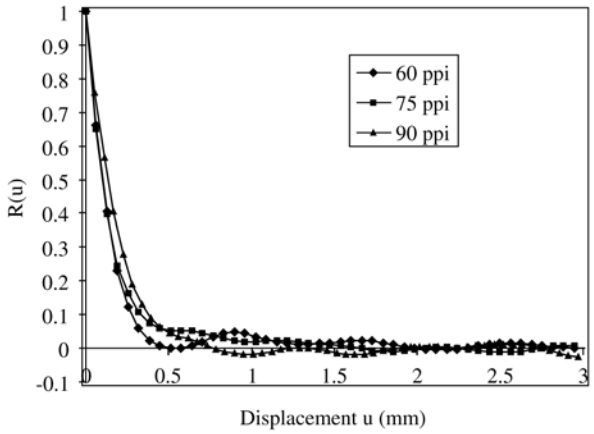

Figure 15. Comparison of the 60, 75 and 90 ppi ceramic foams' normalized autocorrelation.

Table 2. Pore size and porosity of the ceramic foam filters.

pores per inch (ppi)	average pore diameter[(a)] (mm) *present work*	average pore diameter (mm)[16]	porosity (%) *present work*	porosity (%)[16]
60	0.92	1.00	80.8[b]	89.4 ; 87.3
		0.50	87.0[a]	77.1 ; 75.9
		0.24		74.4 ; 73.2
75	0.92	0.42	86.7[b]	84.4 ; 77.6 ; 75.0
		0.16	87.8[a] ; 92.7[a]	73.3 ; 72.6 ; 71.5
90	0.70	0.34	74.4[b]	87.9 ; 73.2 ; 71.5
	0.56		71.5[a] ; 56.8[a]	70.6 ; 68.5

a) Imago analysis 28.3 keV tomography; b) Transept analysis 28.3 keV tomography.

4. Conclusions

This paper shows the potential of X-ray microtomography and image analysis for microstructural characterization.

The Imago software analysis of the ceramic filters produced good results, allowing for the measurement of total porosity as well as detailed pore size distribution, extending the description of this porous media beyond the concept of average pore diameter. The very simple method of microtomography transept analysis also provided good results for the total porosity of the three samples studied. Considering all the methodologies presented at Table 1, the total porosity (%) of the 60, 75 and 90 ppi ceramic foams were (86.7 $\pm$ 2.8)%, (89.1 $\pm$ 2.8)% and (69.5 $\pm$ 8.2)%, respectively, for 95% confidence level. A comparison of the 60 ppi, 75 ppi and 90 ppi ceramic foam samples' normalized autocorrelation showed that they were very close, indicating a similar spatial arrangement with a correlation-length of about 0.30 mm.

Acknowledgments

The authors would like to thank the Brazilian Ministry of Science and Technology (MCT) for its financial support of the PADCT project and the Brazilian Ministry of Education (MEC) for its financial support of the PROCAD/CAPES project.

References

1. Appoloni C.R.; Cesareo R.; *Microscanning and microtomography with X-ray tubes*, RAP. 04.94, CISB, Università Degli Studi di Roma "La Spienza", p. 84, 1994.
2. Macedo A; Vaz C.M.P.; Naime J.M.; Cruvinel P.E., Crestana S. *Powder Technology*, v. 101, p. 178 - 182, 1999.
3. Ioannidis, M.A.; Kwiecien, M.J; Chatzis, I. *J. Petr. Sci. Eng.*, v. 16, p. 251-261, 1996.
4. Quiblier, J.A. *J. Colloid Interface Sci*., v. 98, p. 84-102, 1984.
5. Liang, Z.R.; Fernandes, C.P.; Magnani, F.S.; Philippi, P.C. *Journal of Petroleum Science and Engineering*, v. 21, p. 273-283, 1998.
6. Talukdar, M.S.; Tosaeter, O.; Ioannidis, M.A.; Howard, J.J. *Transport in porous media*, v. 48, p. 101-123, 2002.
7. Bentz, D.P.; Martys, N.S. *Transport in porous media*,

v. 17, p. 221-238, 1994.
8. Santos, L.O.E.; Philippi, P.C.; Damiani, M.C.; Fernandes, C.P. *Journal of Petroleum Science and Engineering*, v. 35, p. 109-104, 2002.
9. Macedo, A.; Cruvinel, P.E.; Inamasu, R.Y.; Jorge, L.A.C.; Naime, J.M.; Torre-Neto, A.; Vaz, C.M.P.; Crestana, S. *Advances in intelligent systems and computer science*, World Scientific and Engineering Society, p. 223-228, 1999.
10. Appoloni, C.R.; Cesareo, R. *Advances in Agricultural Tomography*, EMBRAPA Agricultural Instrumentation, São Carlos - SP, Brazil, p. 31 - 35, 2000.
11. Macedo, A. *Construção e uso de um tomógrafo com resolução micrométrica para aplicações em Ciências do Solo e do Ambiente*, Doctoral thesis, Universidade de São Paulo, Escola de Engenharia de São Carlos, Centro de Recursos Hídricos e Ecologia Aplicada, São Carlos - SP, Brazil, p. 129, 1997.
12. Adler, P.M.; Jacquin, C.G.; Quiblier, J.A. *Int. J. Multiphase Flow*, v. 16, p. 691-712, 1990.
13. Coster, M.; Chermant, J.L.; *Precis D'analyse D'images*. Presses du CNRS, Paris, 1989.
14. Chassery, J.M.; Montanvert, A. *Géometrie Discrète en Analyse d'Images*, Editions Hermes, Paris, 1991.
15. Pöttker, W.E.; Appoloni C.R.; *Radiation Physics and Chemistry*, v. 61, p. 535-536, 2001.
16. Innocentini, M.D.M.; Salvini, V.R.; Coury, J.R.; Pandolfelli, V.C. *Bulletin of the American Ceramic Society*, v. 78, n. 9, p. 78-84, 1999.
17. Lanteajoul, C. *Journal of Microscopy*, v. 161, n. 3, p. 387-404, 1991.